

# Curvature Wavefront Sensing for the Large Synoptic Survey Telescope

Bo Xin,<sup>1,\*</sup> Chuck Claver,<sup>1</sup> Ming Liang,<sup>1</sup> Srinivasan Chandrasekharan,<sup>1</sup> George Angeli,<sup>1</sup> and Ian Shipsey<sup>2</sup>

<sup>1</sup>*Large Synoptic Survey Telescope, 933 N Cherry Ave., Tucson, AZ 85719, USA*

<sup>2</sup>*Department of Physics, University of Oxford, Oxford, UK*

## Abstract

The Large Synoptic Survey Telescope (LSST) will use an active optics system (AOS) to maintain alignment and surface figure on its three large mirrors. Corrective actions fed to the LSST AOS are determined from information derived from 4 curvature wavefront sensors located at the corners of the focal plane. Each wavefront sensor is a split detector such that the halves are 1mm on either side of focus. In this paper we describe the extensions to published curvature wavefront sensing algorithms needed to address challenges presented by the LSST, namely the large central obscuration, the fast  $f/1.23$  beam, off-axis pupil distortions, and vignetting at the sensor locations. We also describe corrections needed for the split sensors and the effects from the angular separation of different stars providing the intra- and extra-focal images. Lastly, we present simulations that demonstrate convergence, linearity, and negligible noise when compared to atmospheric effects when the algorithm extensions are applied to the LSST optical system. The algorithm extensions reported here are generic and can easily be adapted to other wide-field optical systems including similar telescopes with large central obscuration and off-axis curvature sensing.

*OCIS codes:* (010.1080) Active Optics; (010.7350) Wavefront sensing; (110.6770) Telescopes.

<http://dx.doi.org/10.1364/XX.99.099999>

---

\* Corresponding author: [bxin@lsst.org](mailto:bxin@lsst.org)

## 1. Introduction

The Large Synoptic Survey Telescope (LSST) is a new facility now under construction that will survey  $\sim 20000$  square degrees of the southern sky through 6 spectral filters (*ugrizy*) multiple times over a 10-year period [1]. The conduct of the LSST survey is defined by a 2-exposure “visit” lasting  $\sim 39$  seconds having the following pattern: 15s integration plus 1s shutter open/close transitions (16s elapsed time), 2s focal plane array (FPA) readout, 16s exposure, 5s telescope repointing and FPA readout (the last 2s readout is concurrent with the telescope repointing). With this cadence the LSST will observe  $\sim 800$  visits per 8 hour night, producing more than 1600 images and  $\sim 15$  Tbytes per night of data and cover the entire visible sky every 3-4 nights. Construction of the LSST includes an 8-meter class 3-mirror telescope, a 3.2 billion pixel camera, and an extensive computing system for data analysis and archiving. Commissioning of the LSST is expected to begin in late 2019 and full surveying operations at the end of 2022.

The optical system (Figure 1, left) of the LSST is based on a modified Paul-Baker 3-mirror telescope design having an 8.4m primary, 3.4m secondary, and 5.0m tertiary feeding a three-element refractive camera system producing a flat 3.5 degree field-of-view with an effective clear aperture of 6.5m. The mean intrinsic imaging performance of the optical design across the optical spectrum from 320nm to 1150nm is better than 0.1 arcsecond full width at half maximum (FWHM) over the full field of view. The optical design has allowed the primary and tertiary mirrors to be fabricated out of a single substrate. Fabrication of the primary-tertiary (M1M3) mirror pair has recently been completed by the Steward Observatory Mirror Lab.

The overall system image quality budget for the LSST is 0.4 arcsecond FWHM and is allocated between the telescope (0.25”) and camera (0.3”) subsystems. With this image quality budget the LSST’s delivered image quality is dominated by the atmospheric seeing at its site on Cerro Pachon in Chile. For the telescope subsystem, the bulk of its budget allocation is taken up by residual mirror figure errors and thermal and gravity-induced misalignments of the camera and secondary mirror systems. In order to maintain this image quality budget the LSST telescope subsystem utilizes an active optics system (AOS) controlling 50 degrees of freedom (DoF) consisting of 20 bending modes each on the actively supported M1M3 and M2 systems and 5 DoF of rigid body position for the camera and M2.

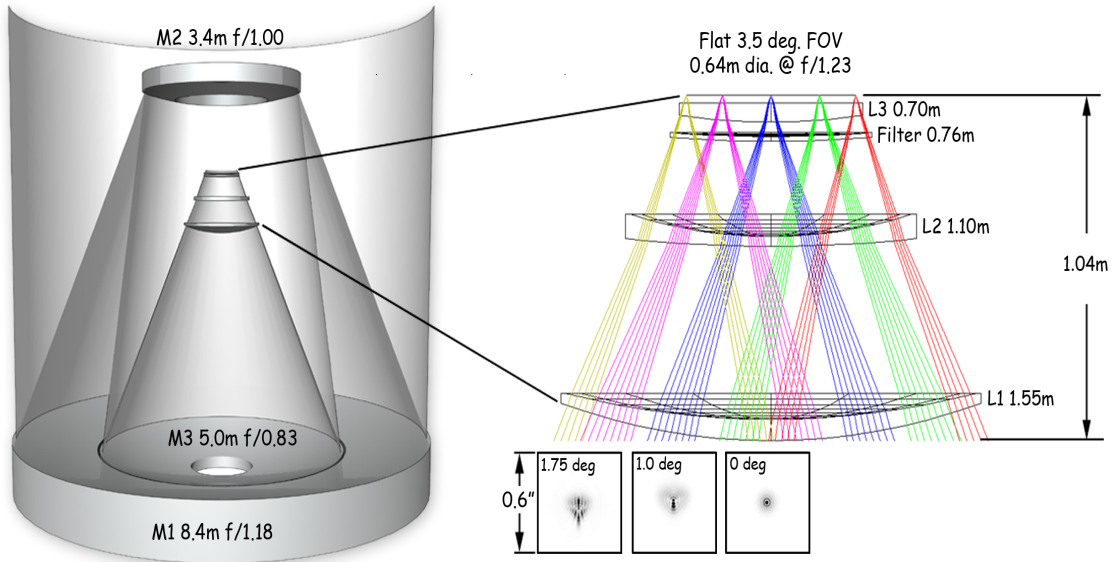


Fig. 1. The 3-mirror telescope optical configuration for the LSST (left) showing the placement of the tertiary mirror within the primary mirror, allowing the two to be fabricated from a single substrate. The camera optics (right) use three fused-silica lenses and a meniscus filter. The r-band image quality (lower right) of the LSST optical system is shown for 0, 1.0 and 1.75 degrees from the optical axis.

By contrast, in the camera subsystem much of its budget allocation is taken up by internal charge diffusion of the  $100\mu\text{m}$ -thick CCDs and overall flatness of the FPA.

Most modern astronomical telescopes use some form of AOS with near-realtime optical wavefront sensing feedback. The most common method for estimating the wavefront in these systems is with a Shack-Hartmann wavefront sensor (SHWFS), e.g. the Magellan telescopes [2] and the VLT [3]. Wide field systems with their fast optical beams make using Shack-Hartmann wavefront sensing problematic for two reasons: 1) To avoid the vignetting effects a pickoff mirror would cause in a fast converging optical beam, the SHWFS would have to be placed near the focal surface. This means these mechanisms would have to be small and within the vacuum cryostat of the imager. 2) Some form of articulation is needed to place the reference star within the SHWFS limited field of view.

Currently operating wide field survey telescopes all use wavefront sensing based on image analysis from area detectors. The VISTA telescope, an infrared survey telescope, utilizes a pair of curvature sensors and forward modeling of low order aberrations to provide optical

feedback [4, 5]. Similarly, the Dark Energy Camera employs 8  $2k \times 2k$  sensors around the focal plane both in and out of focus to forward model the resulting donut images [6]. Curvature wavefront sensing is also in use on several operating telescopes including the 3.5m WIYN [7] and 4m Mayall [8] telescopes at Kitt Peak National Observatory. These telescopes use curvature wavefront sensing to build their AOS look-up tables and to periodically set the operational zero points for the AOS. In each of these systems the number of DoF controlled is limited to focus, misalignment of the instrument or secondary mirror (coma), and one or two forms of primary mirror bending (astigmatism and/or trefoil).

Because LSST uses two actively supported mirror systems and two positioning hexapods, the number of controlled DoF is significantly greater than typically seen in currently operating telescopes. Controlling these DoF requires the ability to estimate higher order properties of the aberrated wavefront, Zernike coefficients  $Z_4 - Z_{22}$  in Noll/Mahajan’s definition [9, 10]. Further, the time constraints imposed by the LSST’s rapid cadence requires that the process of measuring the optical wavefront and maintaining alignment and figure control be highly automated and reliable. For these reasons we have adopted curvature wavefront sensing to provide the optical feedback needed to control the LSST’s AOS.

The layout of the LSST focal plane (Figure 2, left) was developed in part to accommodate the LSST’s wavefront sensing requirements. The science sensors (blue) are arranged in 21 modular “rafts”, each containing 9 CCDs. At four locations are “corner rafts” consisting of two guide sensors (yellow) and one wavefront sensor (green) each. By measuring the field-dependent  $Z_4 - Z_{22}$  at 4 locations we have 76 variables to control 50 DoF.

Curvature wavefront sensing offers some advantages over other wavefront sensing methods for wide field survey telescopes. By relying on equally defocused intra- and extra-focal images, curvature sensing can use area sensors with relatively large fields-of-view. This allows significant flexibility in selecting reference sources to use for the wavefront measurement when the source scenery is constantly changing from one visit to the next with the LSST cadence.

Typically this is achieved through using a beam splitter and delay line or by physically moving the detector. Both of these approaches are problematic for the LSST with its fast  $f$ -number ( $f/1.23$ ) and crowded focal plane. Our design for LSST therefore splits the available wavefront sensor area in two halves (see Figure 2, right), with one 1mm in front of nominal focus and the other 1mm behind. Each half utilizes a  $2k \times 4k$  CCD with  $10\mu\text{m}$  square pixels

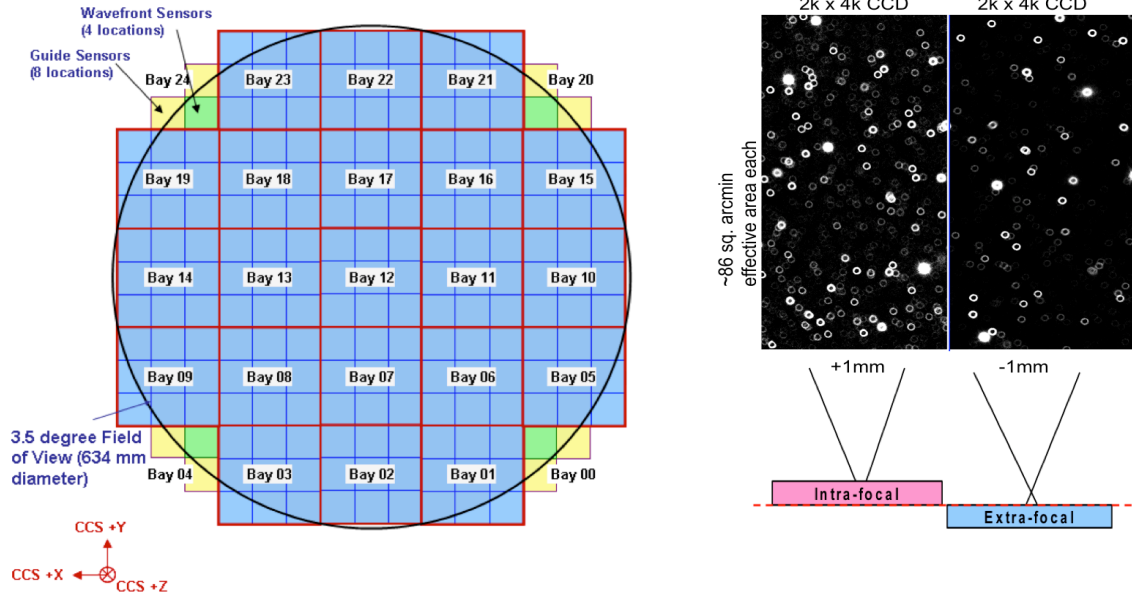


Fig. 2. The focal plane configuration for the LSST (left panel) showing sensors used for science (blue), guiding (yellow), and wavefront sensing (green). Each raft is mounted into a preadjusted grid “bay”. The wavefront sensors are divided into two halves of intra- and extra-focal sensors (right panel). The strategy in making use of multiple stars on each half-chip to obtain a wavefront measurement at each corner is currently under investigation and not discussed in this paper.

providing a  $7 \times 14$  arcminute field of view. With this field of view, the likelihood of acquiring suitable reference stars is near unity even in the low density galactic pole regions [11]. Therefore, no active acquisition of the reference source is required.

There are a variety of algorithms used to estimate the wavefront in curvature wavefront sensing. However, none of them by themselves can work with a wide-field telescope having large central obscuration and off-axis sensors like LSST. Our strategy is to choose two well-established algorithms that are known to work for large  $f$ -number, on-axis systems, implement them as our baseline, then extend them to work with small  $f$ -number and off-axis sensors. As our two baseline algorithms we have chosen the iterative Fast Fourier Transform (FFT) method by Roddier and Roddier [12], and the series expansion technique by Gureyev and Nugent [13]. We found both methods to be accurate and reasonably fast. We note that our extensions to the baseline algorithms can also be used with other curvature sensing algorithms that work for large  $f$ -number and on-axis systems, in order to make them work for small  $f$ -number and off-axis sensors.

In this paper, we describe the development of the curvature wavefront sensing algorithm that measures the wavefront at the 4 corner locations. The paper is organized as follows. In Section 2 we review our baseline algorithms of curvature wavefront sensing, and in Section 3 we discuss the new challenges facing a wide-field and off-axis system like LSST. We also discuss in Section 3 the required modifications to the baseline algorithms in order to overcome these challenges. Section 4 then gives simulation results of unit testing and validations, including analyses of algorithmic noise and atmospheric background.

## 2. Baseline Curvature Sensing Algorithms

The concept of curvature wavefront sensing was first developed and demonstrated by F. Roddier [14]. The underlying idea is to measure the spatial intensity distribution of a star at two positions, one on either side of focus. The derivative of the local surface brightness of the defocused images along the direction of propagation is given by the transport of intensity equation (TIE) [12]:

$$\frac{\partial I}{\partial z} = -(\nabla I \cdot \nabla W + I \nabla^2 W), \quad (1)$$

where  $I$  is the intensity,  $W$  is the wavefront error, and  $z$  is the distance between the conjugate planes of the defocused pupil images.

Assuming the intensity is equal to  $I_0$  everywhere inside the pupil and zero outside, we have the Neumann boundary conditions:

$$\nabla I = -I_0 \hat{n} \delta_c, \quad (2)$$

where  $\delta_c$  is a delta function around the pupil edge. Therefore, the first term in Eq. (1) is localized at the beam edge. Across the beam, the derivative of the local image brightness is proportional to the Laplacian, or curvature, of the wavefront.

As a partial linear differential equation, the TIE can be solved with various methods. In the following 2 subsections we summarize the two methods we have adopted as our baseline algorithms.

### 2.A. Iterative FFT

The iterative FFT algorithm [15] solves the TIE by making use of the Laplacian operator becoming a simple arithmetic operation in Fourier space.

The longitudinal derivative of the intensity can be expressed as

$$-\frac{1}{I_0} \frac{\partial I}{\partial z} = \nabla^2 W - \delta_c \frac{\partial W}{\partial \vec{n}}. \quad (3)$$

We define the wavefront signal  $S$  using the longitudinal derivative normalized by  $I_0$ . As such,  $S$  can be approximated as:

$$S = -\frac{1}{I_0} \frac{\partial I}{\partial z} \approx -\frac{I_1 - I_2}{I_0 \cdot 2\Delta z} \approx -\frac{1}{\Delta z} \frac{I_1 - I_2}{I_1 + I_2}, \quad (4)$$

where the focus offset in the object space (e.g. the pupil) is given by

$$\Delta z = f(f - l)/l, \quad (5)$$

with  $f$  the system focal length, and  $l$  the defocus distance of the intra/extra focal image planes.

It can be shown that if we constrain  $\partial W/\partial \vec{n}$  on the edge,  $\delta_c$  can be absorbed into the Laplacian. An estimate of the Laplacian of the wavefront error can be rewritten as

$$\nabla^2 W \approx S. \quad (6)$$

Using the following property of the Fourier Transform (FT) (see for example page 314 of Ref. 16),

$$FT(\mu, \nu) \{ \nabla^2 W(x, y) \} = -4\pi^2(\mu^2 + \nu^2) FT(\mu, \nu) \{ W(x, y) \}, \quad (7)$$

where  $\mu$  and  $\nu$  are the spatial frequencies, we can solve for  $W$  using the inverse Fourier Transform (*IFT*):

$$W \approx IFT(x, y) \left\{ \frac{FT(\mu, \nu) \{ S \}}{-4\pi^2(\mu^2 + \nu^2)} \right\}. \quad (8)$$

The implementation of the FFT algorithm is shown in Figure 3 (left, boxes 1–8). It involves iteratively applying Equation 8 to estimate the wavefront  $W$ , then setting boundary condition and putting the original wavefront signal,  $S$ , back inside the boundary to obtain a new signal. The algorithm we have described thus far is called the “inner loop”.

As was noted by Roddier and Roddier [12], the method above is only a first order approximation valid for small  $\Delta z$  values, i.e., highly defocused images (see Eq. (5)). The initial solution of the Poisson equation we obtain by the “inner loop” should be used as a first order solution that is further refined in a second iterative process.

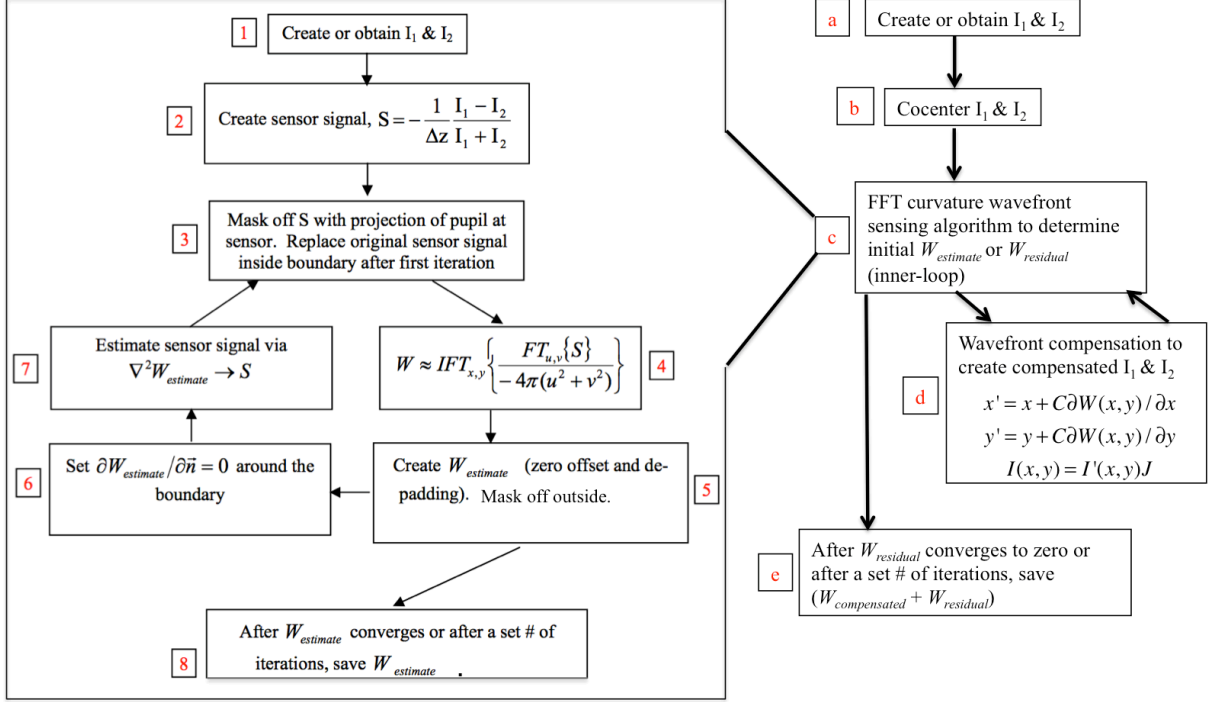


Fig. 3. The block diagram of the iterative FFT algorithm including the “outer loop” image compensation for the estimated wavefront aberrations.

The overall algorithm accuracy can be improved by iteratively removing or compensating for the effects of the estimated wavefront aberrations on the original intra- and extra-focal intensity images and then reapplying the “inner loop” to the corrected images. This “outer loop” (Figure 3 (right, boxes a–e)) is iterated on until the noise level or a given number of iterations is reached. With each iteration of the “outer loop” the estimated residual wavefront is summed with the previous solution to provide the current wavefront estimate.

We compensate/correct the intra- and extra-focal images for the aberrations of the current wavefront estimate by remapping the image flux using the Jacobian of the wavefront in the pupil plane. For this process we let  $R$  be the pupil radius of the telescope and denote the reduced coordinates in the pupil plane as  $x = U/R$  and  $y = V/R$ , where  $U$  and  $V$  are Cartesian coordinates in the pupil plane, and those in the image plane as  $x'$  and  $y'$ . The reduced coordinates in the pupil and image planes are related by [12]

$$x' = x + C\partial W(x, y)/\partial x, \quad (9)$$

$$y' = y + C\partial W(x, y)/\partial y, \quad (10)$$



with

$$C = -\frac{f(f-l)}{l} \frac{1}{R^2}. \quad (11)$$

The intensities in the two planes are related by the Jacobian ( $J$ ) due to flux conservation,

$$I(x, y)/I'(x, y) = J = \begin{vmatrix} \partial x'/\partial x & \partial x'/\partial y \\ \partial y'/\partial x & \partial y'/\partial y \end{vmatrix} \quad (12)$$

Using these relations, given a wavefront estimation from a pair of defocused images, we are able to “restore” the pair of images to a state where the given estimated wavefront aberrations are absent. The new images are then fed to the inner loop (see box c in Figure 3) where the residual wavefront error is estimated. The loop continues until the residual wavefront  $W_{\text{residual}}$  is consistent with zero, or a given number of outer iterations is reached.

Our compensation algorithm has an oversampling parameter, which enables sub-pixel resolution for the mapping between the pupil and image planes. We can choose to improve the compensation performance by increasing the sub-pixel sampling, but at a cost of computation time. Due to the fact that the compensation is based on geometrical ray-tracing, we always compensate on the original defocused images. A feedback gain less than unity is used to prevent large oscillation in the final wavefront estimation, i.e., upon each outer iteration only part of the residual is compensated. To decouple Zernike terms with the same azimuthal frequency, for example, between tip-tilt and astigmatisms, and defocus and spherical aberration, only a certain number of low order Zernike terms are compensated at each outer iteration. After the algorithm has converged on low order terms, higher order terms are added to the compensated wavefront. The tests we show in Section 4 each include 14 outer iterations, with the highest Zernike index of 4, 4, 6, 6, 13, 13, 13, 13, 22, 22, 22, 22, 22, and 22, respectively.

The compensation algorithm also helps identify cases where the geometric limit has been reached. When the compensation procedure results in a negative intensity on the pupil plane, an in-caustic warning flag is set. Here “in-caustic” means rays approaching focus from different points in the pupil cross before the intra focal or beyond the extra focal image plane. This crossing leads to ambiguities in the interpretation of the image intensities and can lead to non-physical negative intensities in the compensated image.

## 2.B. Series Expansion

The series expansion method of solving the TIE is based on the decomposition of the TIE into a series of orthonormal and complete basis functions [13]. Since the outer loop is using the annular Zernike polynomials, it is natural to choose those for the basis, albeit the method would certainly work with any orthonormal basis set.

Let  $\Omega$  be the area of the plane with positive intensity  $I$  and smooth boundary  $\Gamma$ . As such, the TIE can also be written as:

$$\partial_z I = -\nabla \cdot (I\nabla W) \quad (13)$$

$$I(x, y) > 0 \quad \text{inside } \Omega \quad (14)$$

$$I(x, y) = 0 \quad \text{outside } \Omega \text{ and on } \Gamma. \quad (15)$$

Let  $Z_i(x, y)$ ,  $i=1,2,3\dots$  be a set of orthonormal and complete basis functions over the pupil,

$$W(x, y) = \sum_{i=1}^{\infty} W_i Z_i(x, y). \quad (16)$$

Now we multiply Eq. (13) by  $Z_j(x, y)$  and integrate over  $\Omega$ ,

$$\int \int (\partial_z I) Z_j d\Omega = - \int \int \nabla \cdot (I\nabla W) Z_j d\Omega. \quad (17)$$

Integrating by parts, and by taking into account the boundary condition, we get

$$\sum_{i=1}^{\infty} M_{ji} W_i = F_j, \quad (18)$$

where

$$F_j = \int \int (\partial_z I) Z_j d\Omega \quad (19)$$

$$M_{ji} = \int \int I(x, y) \nabla Z_j \cdot \nabla Z_i d\Omega. \quad (20)$$

Therefore,

$$\mathbf{W} = \mathbf{M}^{-1} \mathbf{F}. \quad (21)$$

Each of our baseline algorithms have certain advantages and applications over the other. The wavefront compensation we have discussed for the iterative FFT method can also be used to improve the performance of the series expansion technique, or any other algorithm used to solve the TIE. For detailed analysis of the wavefront structure the iterative FFT is

preferred since it results in a 2-D image of the wavefront. Both methods work with arbitrary pupil geometry, provided that a set of orthonormal basis functions over the pupil can be found. When such basis functions are not available, the accuracy of the series expansion method degrades more because the expansion relies on the orthogonality of the basis, whereas for iterative FFT, the non-orthogonality only makes decomposition of the solved wavefront into the Zernike space problematic. On the other hand, when speed is a concern, the series expansion is the preferred method. With the same number of outer iterations, we found that the series expansion is about 5 times faster than the iterative FFT. We anticipate both methods will be used in LSST during commissioning and engineering (iterative FFT) and routine survey operations (series expansion). In the analyses presented in the rest of the paper, we use the series expansion as the inner-loop, and the wavefront compensation as the outer-loop.

### 3. Algorithm Modifications for LSST

LSST’s optical system poses four algorithmic challenges to using curvature sensing and solving the intensity transport equation for estimating the wavefront error at the entrance pupil: 1) the high central obscuration requires the use of annular Zernike polynomials as the basis set; 2) the fast  $f/1.23$  optical beam results in significant nonlinearity in projecting the wavefront error on the pupil plane; 3) at the location of the wavefront sensors there is significant pupil distortion and vignetting that must be accounted for; and 4) field-dependent variations in the wavefront over the wavefront sensor area must also be accounted for. Our solutions for each of these are given in the discussion that follows.

#### 3.A. Large Central Obscuration

In both the iterative FFT and the series expansion methods, we decompose the wavefront onto a set of orthonormal and complete basis functions. Traditionally, the “standard” filled aperture Zernike polynomials have been chosen for this purpose due to their well-understood properties [9]. When the optical system has non-zero obscuration, the Zernike polynomials are no longer orthogonal. When the obscuration is small, the non-orthogonality does not cause much of a problem. However, when the central obscuration gets large, the non-

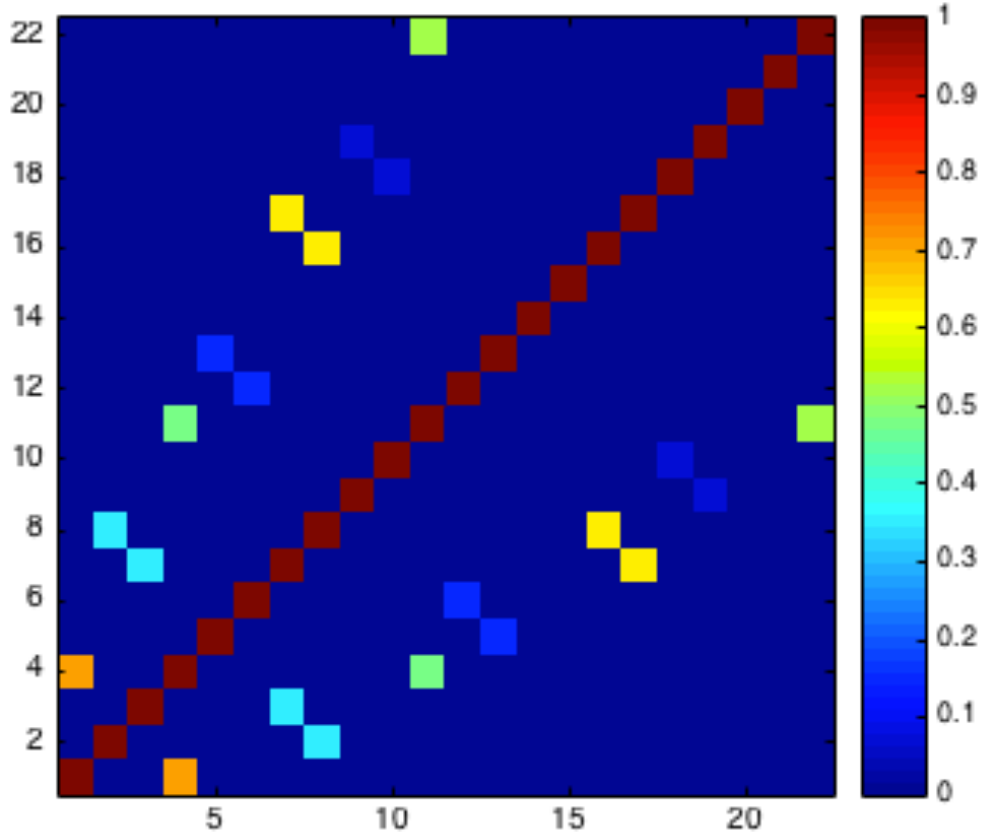


Fig. 4. Orthogonality test of the standard Zernike polynomial on an entrance pupil with 60% obscuration. The  $x$ - and  $y$ - axes are the order of the Zernike polynomials (up to 22).

orthogonality causes a degeneracy problem in the Zernike decomposition. Figure 4 shows the orthogonality test of the standard Zernike polynomial on an LSST-like 60% obscured entrance pupil.

The obvious solution is to use the annular Zernike polynomials [10]. This ensures the orthogonality on the annular pupil. However, note that an obscuration means there is a loss of information. Even with the annular Zernike polynomials, large central obscuration means that the wavefront is harder to measure compared to the case when there is no or small obscuration.

### 3.B. Correcting for Fast $f$ -number

In a fast-beam optical system like LSST the wavefront error defined on the reference sphere at the exit pupil can no longer be projected on the pupil plane in a straightforward, linear

way. The steepness of the fast-beam reference sphere results in non-linear mapping from the pupil ( $x - y$  plane) to the intra- and extra-focal images ( $x' - y'$  plane). Consequently, the intensity distribution on the aberration-free image is no longer uniform and would give rise to anomalous wavefront aberration estimates. This effect also causes the obscuration ratio as seen at the intra- and extra-focal image planes to be different from that on the pupil; thus the linear equations for the mapping between  $x - y$  and  $x' - y'$  (Eqs. 9 and 10) are no longer valid. Therefore, we need to quantify the non-linear fast-beam effect, and be able to remove it so that the corrected images can be processed using the iterative FFT or the series expansion algorithms.

For an on-axis fast-beam system, it can be shown that

$$x' = F(x, y)x + C \frac{\partial W}{\partial x}, \quad (22)$$

$$y' = F(x, y)y + C \frac{\partial W}{\partial y}, \quad (23)$$

with

$$F(x, y) = \frac{m\sqrt{f^2 - R^2}}{\sqrt{f^2 - (x^2 + y^2)R^2}}, \quad (24)$$

where  $m = R'/f/(lR)$  is the mask scaling factor,  $R'$  is the radius of the no-aberration image,  $C$  has been defined in Eq. (11), and the reduced coordinates on the image plane are normalized using the paraxial image radius  $R'/m = lR/f$ , i.e., the radius of the image for a paraxial system with the same  $f$  and  $R$ . Note that flux conservation (Eq. (12)) still holds. The partial derivatives of the Jacobian become

$$\frac{\partial x'}{\partial x} = F(x, y)\left(1 + \frac{x^2 R^2}{f^2 - r^2 R^2}\right) + C \frac{\partial^2 W}{\partial x^2} \quad (25)$$

$$\frac{\partial y'}{\partial y} = F(x, y)\left(1 + \frac{y^2 R^2}{f^2 - r^2 R^2}\right) + C \frac{\partial^2 W}{\partial y^2} \quad (26)$$

$$\frac{\partial x'}{\partial y} = F(x, y) \frac{xy R^2}{f^2 - r^2 R^2} + C \frac{\partial^2 W}{\partial xy} \quad (27)$$

$$\frac{\partial y'}{\partial x} = F(x, y) \frac{xy R^2}{f^2 - r^2 R^2} + C \frac{\partial^2 W}{\partial xy}. \quad (28)$$

With this mapping we are able to fully account for geometric projection effects of the LSST's fast  $f$ -number.

### 3.C. Off-axis distortion and Vignetting Correction

The LSST wavefront sensors are located about  $1.7^\circ$  off the optical axis. On top of the non-linear projection effects due to the small  $f$ -number, the off-axis images are distorted and non-axisymmetric. Since an analytical mapping from the telescope aperture to the defocused image planes is not readily achievable, we instead have developed a numerical solution, representing the mapping between the two sets of coordinates with 2-dimensional 10th order polynomials. The coefficients of the polynomials are determined using least-square fits to the ray-hit coordinates from a grid of rays simulated by the LSST ZEMAX model. The agreement between the fit and the ZEMAX data is better than one percent of a pixel. The gradients and Jacobians are then calculated and implemented in the wavefront compensation code.

Compared to a paraxial model with the same  $f$ -number, the off-axis distortion shifts the ray-hit coordinates on the image planes by up to about 6 pixels, relative to the chief ray, had there been no central obscuration. At the upper right corner of the focal plane, this distortion is symmetric about the  $45^\circ$  line. In contrast, the maximum shifts in the ray-hit coordinates on the image plane caused by 200nm of  $45^\circ$  – astigmatism is about 0.2 pixel.

Because the wavefront sensors are at the edge of the  $3.5^\circ$  field of view, the wavefront images are vignetted. For most parts of the wavefront chip, vignetting is mainly due to the primary and secondary mirrors and increases gradually with field angle. When the field angle gets to about  $1.7^\circ$ , vignetting due to the camera body starts to cause a sharp decrease in the fraction of unvignetted rays. Figure 5 shows intra-focal images on a  $5 \times 5$  grid covering the upper right wavefront chip with field angle ranging from  $1.51^\circ$  to  $1.84^\circ$ .

Vignetting means loss of information on the edge of the pupil, making it harder to recover the wavefront. This is especially true for aberrations like coma, where most of the intensity variations occur near the edge of the image. Furthermore, although neither the iterative FFT nor the series expansion algorithm has requirements on the shape of the pupil, they do rely on decomposition of the wavefront onto the annular Zernike polynomials, which are no longer orthogonal on vignetted pupils. Because the vignetting is relatively small,  $\sim 10\%$ , the deterioration of the wavefront estimation accuracy due to this non-orthogonality has been observed to be small. At the center of the wavefront chip, unit tests using ZEMAX images show no visible increase in estimation uncertainty compared to the on-axis tests.

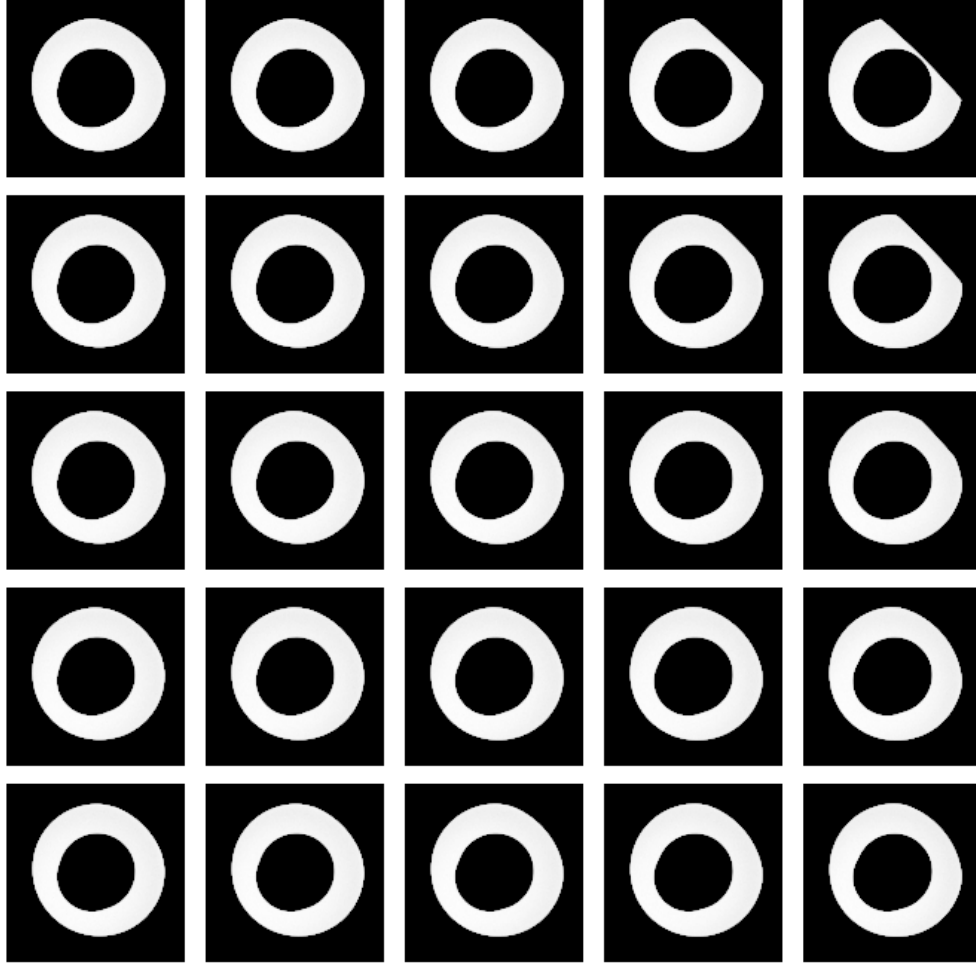


Fig. 5. Intra-focal images on a  $5 \times 5$  grid covering the LSST upper right wavefront chip with field angle ranging from  $1.51^\circ$  to  $1.84^\circ$ . Note that these are ZEMAX simulated images for analysis and testing purposes. In reality, the intra-focal images are acquired on half of the wavefront chip only.

### 3.D. Field-Dependent Corrections

The split sensor design of LSST introduces two additional potential sources for error. First, the TIE used in curvature sensing requires that the total flux in the intra- and extra-focal images are the same. Using different sources for the intra- and extra-focal images in general will violate this requirement. This can be largely overcome by local background subtraction and normalizing to the source flux during the processing of the intra- and extra-focal images prior to solving for the wavefront.

Second, the curvature sensing method assumes that both the intra- and extra-focal images

contain the same optical properties (aberrations and pupil geometry). Because the intra- and extra-focal sources will come from different parts of the field of view they will not have identical optical properties.

The off-axis geometric distortions are field-dependent as are the telescope intrinsic aberrations and vignetting. The off-axis correction we discussed previously corrects intensity variations, regardless of their source, be it from the off-axis distortion or the field-dependent telescope intrinsic aberrations. When we make the off-axis correction, we always do so referenced to a common field coordinate at the center of the wavefront sensing area, regardless of the source's original location. Thus, the off-axis correction removes both the effects of field dependent geometric distortion and intrinsic design aberrations.

The vignetting pattern still varies by field. To avoid anomalous signal due to the difference in vignetting from entering the wavefront estimation results, we mask off the intra- and extra-focal images using a common pupil mask, which is the logical AND of the pupil masks at the intra- and extra-focal field positions.

#### **4. Algorithm Validation and Unit Testing**

We have applied many levels of unit testing on the LSST wavefront sensing algorithms using images with and without the effects of atmospheric turbulence. Examples of these tests and their results are provided below.

##### **4.A. Paraxial Unit Testing**

We have performed comprehensive tests with on-axis images created in ZEMAX using a paraxial lens model, with  $f$ -number ranging from 1.3 to 4; image space defocus from 1mm to 5mm; and obscuration ratios from 0 (filled) to 60%. One example of such tests is given in Figure 6. The results agree nicely with the ground truth from ZEMAX.

Our wavefront estimation algorithm performs very well. For the single-Zernike-term tests, each Zernike mode runs into caustic at a different aberration magnitude. For  $f/1.23$ , 1mm image space defocus, with RMS wavefront aberration below 1.5 microns, the only problematic modes are the 5th order astigmatisms.



#### 4.B. LSST On- and Off-axis

Unit test results using ZEMAX simulated images for various Zernike terms at different magnitudes show that the fast-beam correction algorithm is very successful. To facilitate algorithm testing, the telescope intrinsic aberrations have been compensated using a phase screen, before applying the known aberration under test.

One example of such tests is given in Figure 7. The intra- and extra-focal images are taken at the center of the focal plane. In this example, the aberration present is 0.5 wave (wavelength is 770nm) of Z11 (spherical aberration). The estimated Z11, as shown in Figure 7, agrees nicely with the ground truth. All other Zernike terms have magnitudes of no more than  $\sim 20\text{--}30\text{nm}$ .

We have also performed unit tests using ZEMAX simulated LSST off-axis images with various Zernike terms at different magnitudes. One example of such tests, where 2 waves (wavelength is 770nm) of Z5 ( $45^\circ$  astigmatism) is applied, is shown in Figure 7. The intra- and extra-focal images are taken at field position ( $1.185^\circ, 1.185^\circ$ ), corresponding to the center of one of the LSST wavefront sensors. Vignetting is clearly visible in these images. Again, the input aberration is recovered, as shown in Figure 7. All other Zernike terms have magnitudes very close to zero. Tests are also performed using images simulated by the LSST Photon Monte Carlo Simulator [17]. A similar level of agreement between the measured wavefront and the truth is observed.

As another set of tests, the ZEMAX model is used including all intrinsic aberrations and various individual perturbations at the 4 corner wavefront sensor locations. Figure 8 shows an example at the field angle of  $(-1.185^\circ, 1.185^\circ)$ , where the secondary mirror has been decentered by 0.5mm.

#### 4.C. Algorithm Linearity

By varying the controlled degrees of freedom of the telescope model and repeating the wavefront measurements, good algorithmic linearity has been observed within the geometric limit. One example of such tests is shown in Figure 9. When the secondary mirror is tilted by incremental amounts, and all other degrees of freedom of the telescope stay unperturbed, the wavefront Zernikes ( $45^\circ$ -astigmatism shown) change linearly. The linearity starts to

degrade in proximity of the geometric limit. Similar behavior has also been observed for other degrees of freedom of the system.

#### 4.D. Covariance Analysis

The atmospheric covariance is computed for 15-second time integrated atmospheres generated using the Arroyo library [18]. Six layers of Kolmogorov phase screens at various heights are simulated. Based on historic DIMM data at Cerro Pachon, and the current understanding on its outer scale, we use  $r_0 = 17\text{cm}$  and assume infinite outer scale.

The same time-integrated phase screens used for the atmosphere covariance are then applied to a ZEMAX ray trace model in order to evaluate the importance of algorithm noise with respect to atmosphere noise in estimating the wavefront. For each time-integrated phase screen instance, ZEMAX is used to generate intra- and extra-focal image pairs at each of the 4 wavefront sensors. These images are then processed through the LSST specific curvature algorithms to estimate the wavefront coefficients. Compared to the calculated coefficients from atmosphere alone (ideal sensor), the results from estimating the wavefront using the simulated sensors are similar, indicating that the covariance is dominated by the atmospheric contribution and not the wavefront sensing algorithms. The plots in Figure 10 show the diagonal entries (19 entries for each field point, corresponding to the Zernike terms estimated) and the singular values of the covariance matrix; the largest singular values most important for estimating the misalignment of the telescope are almost identical.

### 5. Summary, Conclusions, and Future Work

Extensions to two curvature wavefront sensing algorithms for LSST have been developed. The underlying algorithms considered are the iterative FFT method by the Roddiers [12] and the series expansion based method by Gureyev and Nugent [13]. These are well-established methods that have been proven to work well for paraxial systems. Several modifications are needed to make them work for LSST, to overcome challenges including a highly obscured pupil, the fast  $f$ -number, pupil distortion and vignetting at the field corners, and variation of the wavefront over the area covered by the split-sensors. Our baseline algorithm for use in routine operations is the series expansion method, due to its higher computational efficiency.

Extensive simulations have been performed using images generated by ZEMAX and the LSST Photon Monte Carlo simulator [17].

Integrated modeling of the LSST AOS, including the optimal control of the system, as well as adapting the algorithms to be used by several other operating telescopes, is reported in [19]. As the LSST construction progresses we are also looking into alternative wavefront sensing algorithms, such as the forward modeling technique used by DECam, and the PSF-based technique used by VST, to compare their performance to the results shown here.

This is the first of a series of papers being planned on the Active Optics System of LSST. The following topics are planned to be discussed in subsequent papers hence not included here: 1) the validation of the algorithms presented in this paper using real data taken at major operating telescopes; 2) the LSST alignment strategy, the tomographic optical reconstruction, and the telescope control algorithm; 3) the general functionality of the LSST active optics systems (AOS) and the prototype processing pipeline we are using to develop a full simulation of the LSST AOS operation.

### **Acknowledgments**

LSST project activities are supported in part by the National Science Foundation through Cooperative Support Agreement (CSA) Award No. AST-1227061 under Governing Cooperative Agreement 1258333 managed by the Association of Universities for Research in Astronomy (AURA), and the Department of Energy under contract with the SLAC National Accelerator Laboratory. Additional LSST funding comes from private donations, grants to universities, and in-kind support from LSSTC Institutional Members.

### **References**

- [1] The LSST Collaboration, “LSST: from Science Drivers to Reference Design and Anticipated Data Products,” <http://www.arxiv.org/abs/0805.2366> (2008).
- [2] P. L. Schechter, G. S. Burley, C. L. Hull, M. Johns, H. M. Martin, S. Schaller, S. A. Sackett, and S. C. West, “Active optics on the Baade 6.5-m (Magellan I) Telescope,” *Proc. SPIE* **4837**, 619–627 (2003).

- [3] S. Guisard, L. Noethe, and J. Spyromilio, “Performance of Active Optics at the VLT,” Proc. SPIE **4003**, 154–164 (2000).
- [4] D. L. Terrett, N. Bissonauth, V. Graffagnino, M. Stewart, and W. J. Sutherland, “Active Optics and Auto-guiding Control for VISTA,” Proc. SPIE **5496**, 129–137 (2004).
- [5] P. Clark, P. Berry, R. G. Bingham, N. Bissonauth, M. Caldwell, N. A. Dipper, C. N. Dunlop, D. M. Henry, P. Luke, R. M. Myers, and D. J. Robertson, “Wavefront Sensing within the VISTA Infrared Camera,” Proc. SPIE **5499**, 379–386 (2004).
- [6] A. Roodman, K. Reil, and C. Davis, “Wavefront Sensing and the Active Optics System of the Dark Energy Camera,” Proc. SPIE **9145**, 914516 (2014).
- [7] N. A. Roddier, D. R. Blanco, L. W. Goble, and C. A. Roddier, “WIYN Telescope Active Optics System,” Proc. SPIE **2479**, 364–376 (1995).
- [8] C. F. Claver, S. E. Bulau, D. Mills, and E. T. Pearson, “Active Optics Upgrade to the KPNO 4-m Mayall Telescope,” Proc. SPIE **4003**, 136–145 (2000).
- [9] R. Noll, “Zernike polynomials and atmospheric turbulence,” J. Opt. Soc. Am. **66**, 207–211 (1976).
- [10] V. N. Mahajan, “Zernike annular polynomials for imaging systems with annular pupils,” J. Opt. Soc. Am. **71**, 75–85 (1981).
- [11] A. M. Manuel, , D. W. Phillion, S. S. Olivier, K. L. Baker, and B. Cannon, “Curvature wavefront sensing performance evaluation for active correction of the Large Synoptic Survey Telescope (LSST),” Optics Express **18**, 1528–1552 (2010).
- [12] C. Roddier and F. Roddier, “Wave-front reconstruction from defocused images and the testing of ground-based optical telescopes,” J. Opt. Soc. Am. A **10**, 2277–2287 (1993).
- [13] T. Guruyev and K. Nugent, “Phase retrieval with the transport-of-intensity equation. ii. orthogonal series solution for nonuniform illumination,” J. Opt. Soc. Am. A **13**, 1670–1682 (1996).
- [14] F. Roddier, “Curvature sensing and compensation: a new concept in adaptive optics,” Applied Optics **27**, 1223–1225 (1988).
- [15] F. Roddier and C. Roddier, “Wavefront reconstruction using iterative fourier transforms,” Applied Optics **30**, 1325–1327 (1991).
- [16] J. Gaskill, *Linear Systems, Fourier Transforms, and Optics* (Wiley, 1978).

- [17] J. R. Peterson, J. G. Jernigan, S. M. Kahn, A. P. Rasmussen, E. Peng, Z. Ahmad, J. Bankert, C. Chang, C. Claver, D. K. Gilmore, E. Grace, M. Hannel, M. Hodge, S. Lorenz, A. Lupu, A. Meert, S. Nagarajan, N. Todd, A. Winans, and M. Young, “Simulation of Astronomical Images from Optical Survey Telescopes Using a Comprehensive Photon Monte Carlo Approach,” *ApJS* **218**, 14 (2015).
- [18] M. Britton, “Arroyo,” *Proc. SPIE* **5497**, 290–300 (2004).
- [19] G. Z. Angeli, B. Xin, C. Claver, D. MacMartin, D. Neill, M. Britton, J. Sebag, and S. Chandrasekharana, “Real Time Wavefront Control System for the Large Synoptic Survey Telescope (LSST),” *Proc. SPIE* **9150**, 91500H (2014).

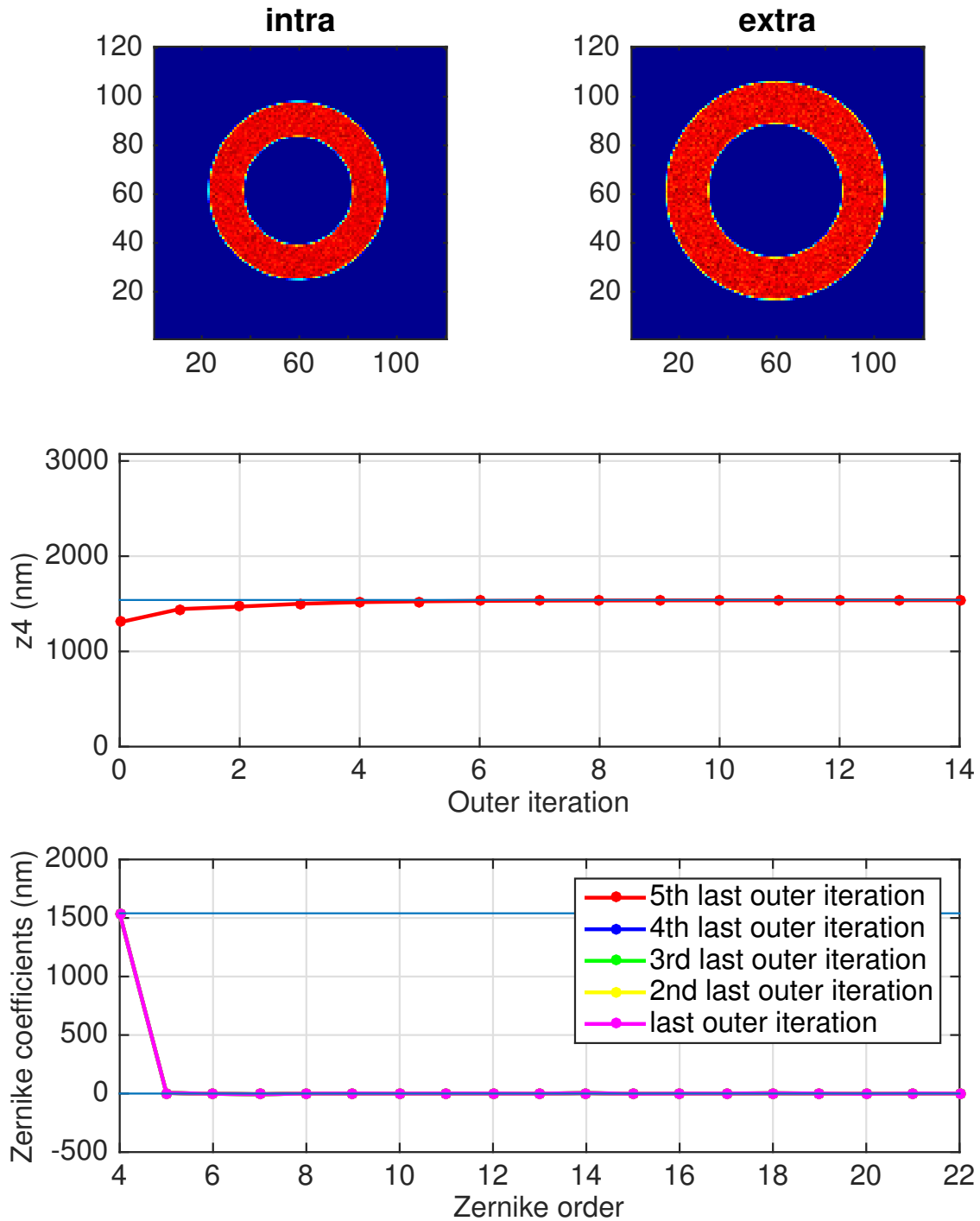


Fig. 6. An example of a paraxial lens unit test for focus ( $Z_4$ ). The top row shows the input images. The middle row shows how the estimated  $Z_4$  converges to the input value. The final annular Zernike composition is shown at the bottom. Note that on the bottom plot, we show results from the last five outer iterations. These curves are on top of each other, which shows good convergence.

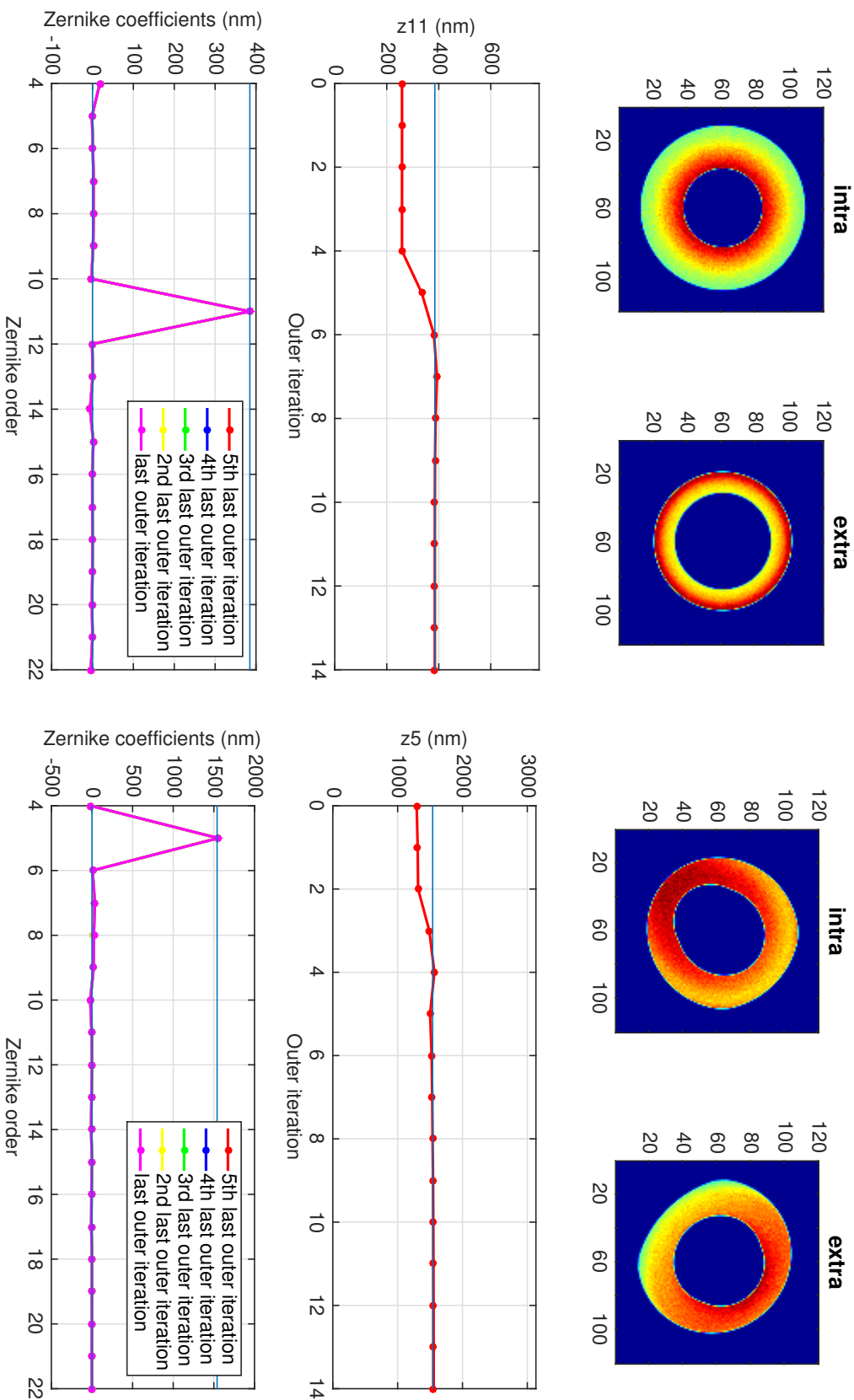


Fig. 7. Additional unit testing is done using a ZEMAX model of the LSST optical system. Two examples are shown for spherical aberration (Z11) on-axis (left) and astigmatism (Z5) at the center of one of the off-axis wavefront sensors. The formatting of the figure is the same as Figure 6. Note that Z11 is compensated in the outer loop starting the 5th iteration, and Z5 starting the 3rd iteration. Note that on the bottom plots, we show results from the last five outer iterations. These curves are on top of each other, which shows good convergence.

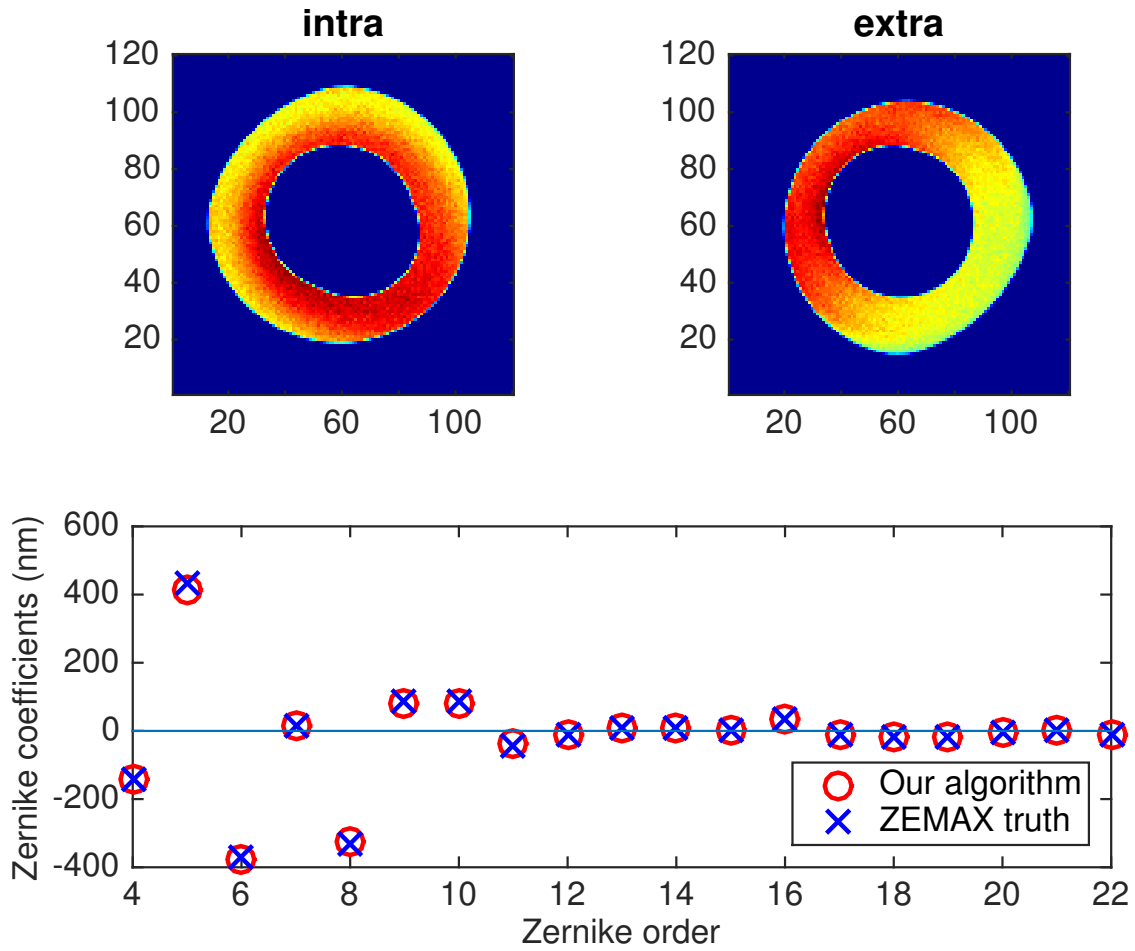


Fig. 8. ZEMAX simulation at the field angle of  $(-1.185^\circ, 1.185^\circ)$  containing all intrinsic aberrations plus a decenter of 0.5mm in the secondary mirror. The recovered aberration coefficients (red circles) are in excellent agreement with the ZEMAX-calculated coefficients (blue crosses).



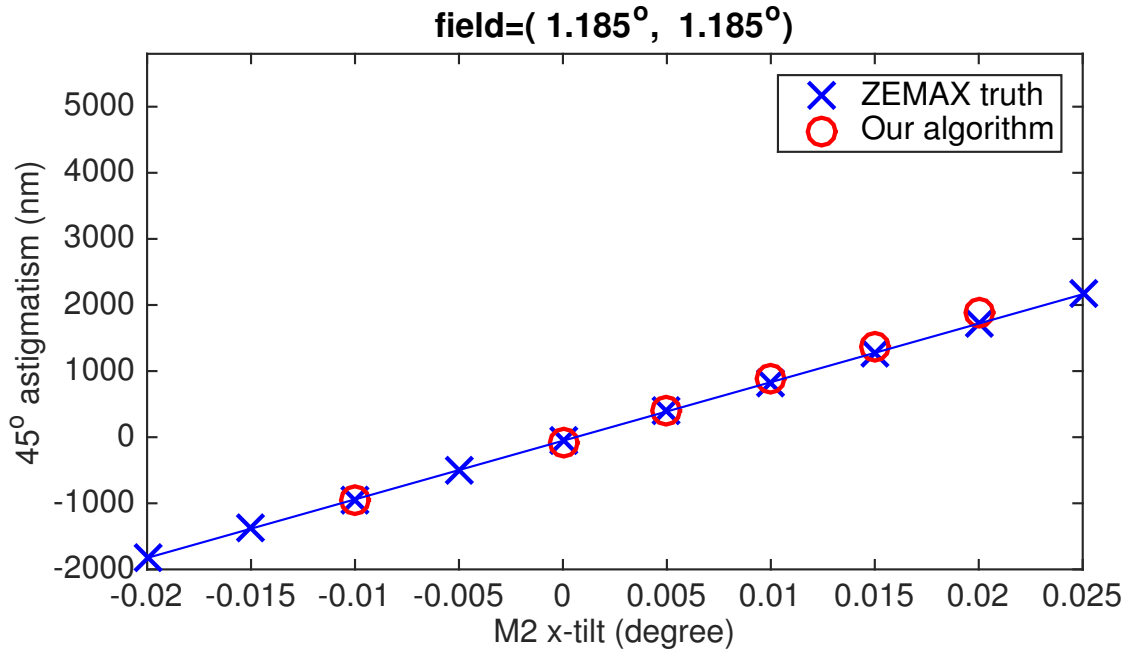


Fig. 9. ZEMAX-calculated wavefront (blue crosses) and the recovered wavefront (red circles) at one of the four corners of the focal plane. The recovered aberration coefficients start to deviate from linearity in proximity of the geometric limit.

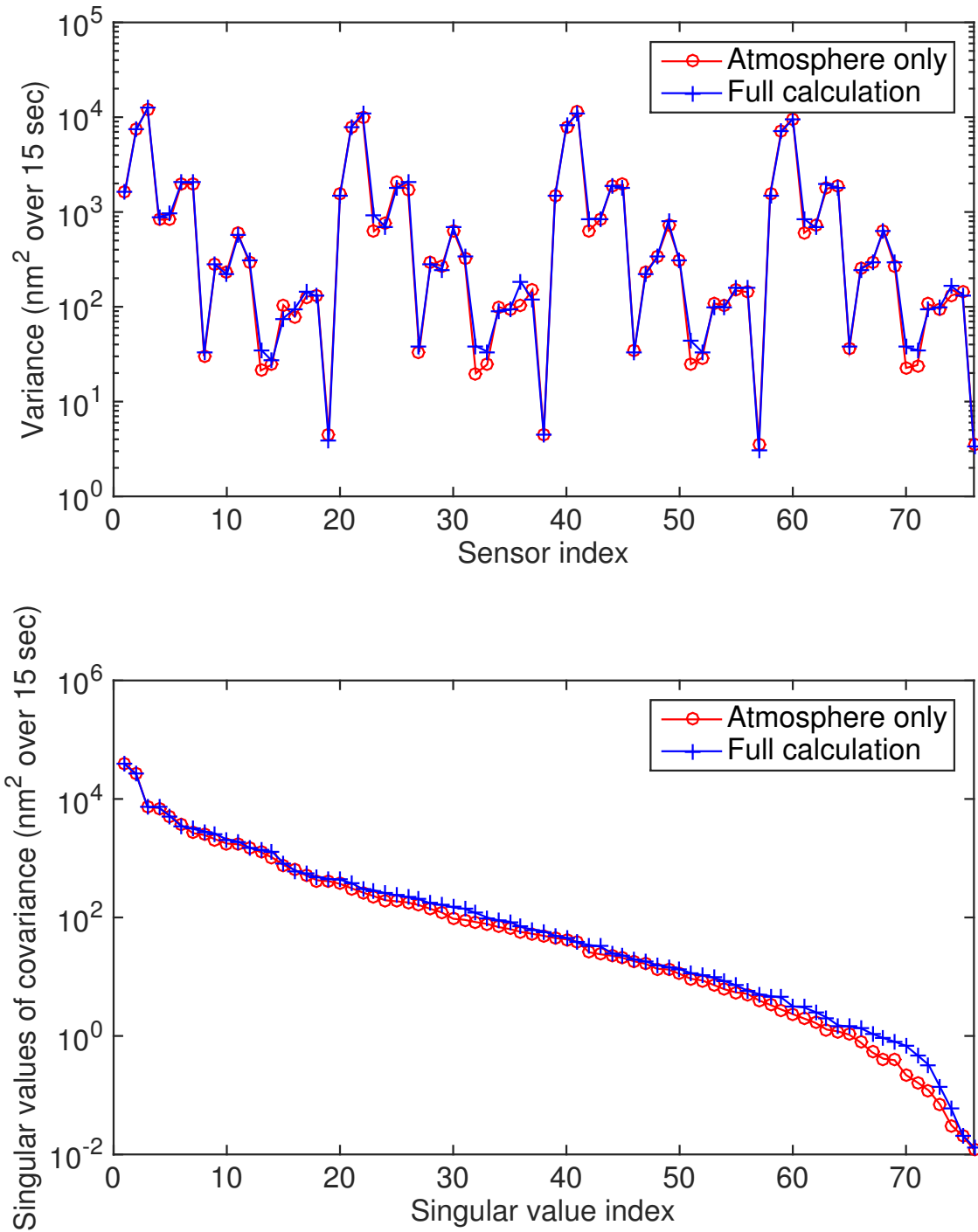


Fig. 10. The nearly identical covariance and singular values of the ideal sensor (atmosphere only) and fully simulated and processed images show that the noise from the atmosphere is dominant. The sensor index ranges between 1 and 76, corresponding to the wavefront Zernike coefficients Z4–Z22 at the four corners.